

New iron-based multiferroics with improper ferroelectricity

Jin Peng¹, Yang Zhang¹, Ling-Fang Lin¹, Lin Lin², Meifeng Liu^{2,3}, Jun-Ming Liu^{2,4} and Shuai Dong¹

¹ School of Physics, Southeast University, Nanjing 211189, People's Republic of China

² Laboratory of Solid State Microstructures and Innovative Center of Advanced Microstructures, Nanjing University, Nanjing 210093, People's Republic of China

³ Institute for Advanced Materials, Hubei Normal University, Huangshi 435002, People's Republic of China

⁴ Institute for Advanced Materials, South China Normal University, Guangzhou 510006, People's Republic of China

E-mail: sdong@seu.edu.cn

Received 26 January 2018, revised 3 April 2018

Accepted for publication 9 May 2018

Published 23 May 2018



Abstract

In this contribution to the special issue on magnetoelectrics and their applications, we focus on some single phase multiferroics, which have been theoretically predicted and/or experimentally discovered by the authors in recent years. In these materials, iron is the common core element. However, these materials are conceptually different from the mostly-studied BiFeO₃, since their ferroelectricity is improper. Our reviewed materials are not simply repeating one magnetoelectric mechanism, but cover multiple branches of improper ferroelectricity, including the magnetism-driven ferroelectrics, geometric ferroelectric, as well as electronic ferroelectric driven by charge ordering. In this sense, these iron-based improper ferroelectrics can be an encyclopaedic playground to explore the comprehensive physics of multiferroics and magnetoelectricity. Furthermore, the unique characteristics of iron's 3d orbitals make some of their magnetoelectric properties quite prominent, comparing with the extensively-studied Mn-based improper multiferroics. In addition, these materials establish the crossover between multiferroics and other fields of functional materials, which enlarges the application scope of multiferroics.

Keywords: multiferroics, improper ferroelectricity, iron oxide, iron selenide, iron fluoride

(Some figures may appear in colour only in the online journal)

1. Introduction

1.1. What are improper ferroelectrics

Ferroelectrics are important functional materials, playing an irreplaceable role in sensors, information storage, transducers, and other applications. Magnetic materials are even more extensively used, especially in the information storage area. Generally speaking, multiferroics denote a class of materials that combine these two different characteristics. A more rigorous definition of a multiferroic material is the simultaneous presentation of more than one primary ferroic order parameter in a single phase [1]. The coexisting and crossover

between ferroelectricity and magnetism not only generates emergent physics, but also provides more functionalities for applications, e.g. electric control of magnetism. Therefore, the field of multiferroic materials and magnetoelectricity is quite attractive and great progress has been made since the beginning of the new century [2–7].

Based on the origin of ferroelectricity, ferroelectrics can be classified into two families: proper ferroelectrics and improper ferroelectrics. The ferroelectrics that have been studied and applied to industries in the past century are basically proper ferroelectrics. Ferroelectricity originates from 'ferroelectric active' ions (e.g. those with the d^0 configuration or with the $6s^2$ lone pair), as found in BiFeO₃, PbTiO₃, and Pb(Fe_{1/2}Nb_{1/2})O₃.

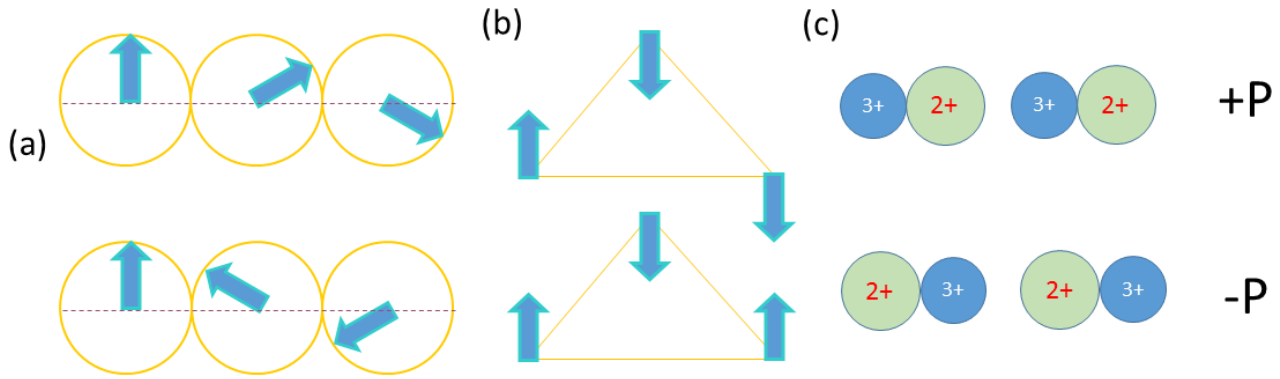


Figure 1. Illustration of three types of improper multiferroics. (a) Magnetic ferroelectrics; (b) geometric ferroelectrics; (c) electronic ferroelectrics. The top and bottom panes denote the positive and negative ferroelectric state.

Although most of the proper ferroelectrics are not magnetic, there are exceptions, such as BiFeO_3 [8].

Improper ferroelectrics form an emerging area with the research upsurge of multiferroic materials. Most improper ferroelectrics are multiferroics, although not all. Improper ferroelectricity is not caused by ‘ferroelectric active’ ions, but the phase transitions of other order parameters, e.g. structural transition (the so-called geometric ferroelectricity), charge-ordering (the so-called electronic ferroelectricity), or magnetic ordering (the so-called magnetic ferroelectricity) [3].

Magnetic ferroelectrics are achieved by some special magnetic orders, such as spiral magnetic ordering as shown in figure 1(a). The displacement of electronic cloud and/or ions can be achieved via the spin–orbit coupling and/or spin-lattice coupling. These materials are also called the type-II multiferroics [9]. The representative material is orthorhombic TbMnO_3 [10].

Geometric ferroelectricity exists in some special lattices with geometric frustration, as shown in figure 1(b). In these materials, ferroelectricity is generated by collaborative multiple nonpolar modes of lattice distortion. Hybrid improper ferroelectrics, which have attracted great attentions recently, also belong to the category of geometric ferroelectrics [11]. Some of these materials are nonmagnetic. However, since transition metal elements are mostly magnetic, most geometric ferroelectrics are multiferroics. The representative material is hexagonal YMnO_3 [12, 13].

Electric dipoles and eventual ferroelectricity can be achieved via charge ordering, leading to so called electronic ferroelectrics [14]. Many transition metal ions have multiple valence states. In some special lattice environments, some elements can have ordered two valence states, forming the charge ordering, as illustrated in figure 1(c). Some charge ordering can be switched between two ordered states, giving rise to ferroelectricity. The representative material is $\text{Pr}_{0.5}\text{Ca}_{0.5}\text{MnO}_3$ [14].

These three types of improper ferroelectrics are mostly magnetic (although there are a few exceptions in geometric ferroelectrics, such as $\text{Ca}_3\text{Ti}_2\text{O}_7$), so they are mostly multiferroics, which generally have magnetoelectric coupling.

1.2. Magnetoelectricity in improper multiferroics

Magnetoelectricity is the correlation between magnetic moment and electric dipole moment. In particular, positive magnetoelectric effect means that the electric dipole moment can be controlled by magnetic field, while the inverse magnetoelectric effect denotes that the control of magnetic moment is by an electric field. The magnetoelectric coupling effect has valuable applications, especially the inverse magnetoelectric effect. The control of magnetic moment by electric field can be energy conservative and efficient. It can overcome the technical bottleneck of current magnetic storage and ferroelectric storage. Magnetoelectric couplings widely exist in single phase bulks, surfaces/interfaces, even in nonmagnetic and nonferroelectric topological insulators [6]. However, the magnetoelectric coupling effects are very weak in most of these systems.

Multiferroics are an ideal platform for the pursuit of strong magnetoelectric coupling because of its intrinsic magnetism and electric dipoles. However, the general mutual exclusion between magnetic moment and electric dipole at the quantum level makes the pursuit of desirable multiferroic materials a challenging problem in condensed matter physics.

For those proper ferroelectrics with magnetism, such as BiFeO_3 , the magnetic and ferroelectric properties originate from independent order parameters. Thus the Landau free energy of the phase transitions in these systems can be abstractly expressed as:

$$F(\mathbf{P}, \mathbf{L}) = \alpha_{\text{Fe}} \mathbf{P}^2 + \beta_{\text{Fe}} \mathbf{P}^4 + \dots + \alpha_{\text{AFM}} \mathbf{L}^2 + \beta_{\text{AFM}} \mathbf{L}^4 + \dots, \quad (1)$$

where \mathbf{P} is the ferroelectric order parameter; \mathbf{L} is the antiferromagnetic (AFM) order parameter; α/β are corresponding coefficients. Therefore, these systems can easily achieve good magnetic/ferroelectric properties. For example, BiFeO_3 has a large ferroelectric polarization ($\sim 90 \mu\text{C cm}^{-2}$), high ferroelectric transition temperature ($\sim 1100 \text{ K}$), and high magnetic transition temperature ($\sim 660 \text{ K}$) [15]. However, due to the independency of magnetic and ferroelectric order parameters, these properties must be coupled by high-order effects, e.g. indirect and weak magnetoelectric coupling via lattice

distortions. Recent theoretical work found that a small portion of BiFeO₃ polarization is improper [16]. This kind of multiferroics can be considered as magnetoelectric composites in the atomic scale.

In contrast, it is hopeful to realize strong magnetoelectric coupling in improper ferroelectrics. The essence is to ‘down-grade’ the ferroelectric order parameter from the primary one to an dependent order parameter controlled by others.

In magnetic ferroelectrics represented by TbMnO₃, the magnetic order (mostly AFM order) is a primary order parameter, while ferroelectricity is a derivative of magnetic order. Therefore, the ferroelectric phase transition temperature is always equal to the magnetic ordering temperature. Thus ferroelectricity can be controlled by tuning magnetism.

In geometric ferroelectrics represented by hexagonal YMnO₃, the electronic polarization (distortion model Γ_2^-) is a derivative of the two collaborative non-polar lattice distortion modes (K_1 : trimer of Mn triangular lattice; K_3 : tilting of O₆ octahedral). Due to the strong order parameters of K_1 and K_3 modes, the ferroelectric transition temperature is very high (basically all above room temperature). Polarization is usually in the order of 10 $\mu\text{C cm}^{-2}$. Meanwhile, the K_3 mode also controls the residual magnetic moment of canting antiferromagnetism. Therefore, the K_3 degree of freedom can regulate magnetism and electric properties simultaneously. Unlike proper ferroelectricity, the polarization of geometric ferroelectrics show hydrostatic pressure and thickness dependence in film sample [17–19].

In electronic ferroelectrics represented by Pr_{1/2}Ca_{1/2}MnO₃, ferroelectricity is due to the coexistence of site-charge-ordering and bond-charge-ordering. It depends on the special charge ordered electronic configuration. Meanwhile, magnetism is also dependent on the electronic configuration. Therefore, the control of the electronic configuration can regulate magnetism and electric properties simultaneously.

In short, if the ferroelectric order parameter can be ‘down-graded’ to the derivative level of other order parameters, it may become easier to be controlled and more closely related to magnetism.

1.3. Improper multiferroics: from manganese-based to iron-based

As mentioned above, one can notice that many improper ferroelectrics are Mn-based oxides. The first magnetic ferroelectric material is TbMnO₃. The first geometric ferroelectrics is hexagonal YMnO₃, and the first candidate of electronic ferroelectrics is Pr_{1/2}Ca_{1/2}MnO₃. These Mn-based oxides cover all three known mechanisms of improper ferroelectricity. Study on these Mn-based oxides can establish the framework of improper ferroelectricity. Therefore, these materials have been extensively studied over the past fifteen years.

Why are the Mn-based oxides so ‘magic’? First, Mn ions have multiple stable valence states in oxides: +2, +3, +4, as well as large magnetic moments correspondingly. For other 3d elements, Sc and Zn have neither multiple stable valence states nor magnetic moments; Ti, V, Co, and Ni do not have magnetic moment in all valence states.

Second, Mn has good chemical activity. Mn-based oxides display abundant crystal structures, including quasi-one dimensional, quasi-two dimensional, three-dimensional, square lattice and triangular lattice. It offers a fertile ground for improper ferroelectrics.

Third, the multiple stable valence states is the prerequisite for the formation of charge ordering, for example, Mn³⁺/Mn⁴⁺ can coexist in several kinds of systems.

Finally, the 3d orbital of Mn is the source of magnetic frustration. For example, in the O₆ octahedral, the 3d orbital splits into triplet t_{2g} levels and doublet e_g levels. For the most common Mn³⁺, t_{2g} orbital is half occupied at the high spin state, and e_g is partially occupied. Therefore, t_{2g} electrons prefer AFM interactions, and the e_g electrons prefer the ferromagnetic coupling. A variety of complex magnetic orders can be achieved via the competition between multiple exchanges [20].

This topical review will focus on iron-based improper ferroelectrics. Compared with Mn-based improper ferroelectrics, the Fe-based ones own similar advantages.

First, iron also has multiple stable valence states in ionic crystals. The most common ones are +2 and +3 although +4/+5 also exist. Similar to Mn ions, Fe ions are generally at the high spin states, leading to large magnetic moments. Fe element also has good chemical activity and varies crystal structures. Typical crystal fields and corresponding electronic configurations are shown in figure 2. It is not difficult to find out that these systems are also an ideal platform for the research of improper ferroelectrics. Iron-based improper ferroelectrics also cover geometric ferroelectrics, magnetic ferroelectrics, and electronic ferroelectrics.

The iron-based improper ferroelectrics also have several advantages compared with the Mn-based improper ferroelectrics. Iron’s 3d orbital has stronger Coulomb repulsion U than Mn. It has narrower 3d band and is much easier to form Mott insulating state. Enhanced correlation strength will also help to improve exchange interaction and enhance the magnetic transition temperature. For example, magnetic ordering temperature of rare-earth manganite RMnO₃ is generally below 200 K [20], while the RFeO₃ become magnetic ordered above room temperature [21]. From this point of view, the low common drawbacks of Mn-based improper ferroelectrics, such as high leakage and low magnetic ordering temperatures, may be solved in Fe-based compounds.

Also due to larger Coulomb repulsion U and narrower d band, charge ordered state is very common in iron-based compound. Further, different valence states (Fe²⁺/Fe³⁺ or Fe³⁺/Fe⁵⁺) are completely separated. In contrast, different valence states in manganese oxides (Mn³⁺/Mn⁴⁺) are not completely separated [22].

Last but not least, due to the discovery of iron-based superconductors, iron sulfides, iron selenides, iron pnictides and other non-oxides have been widely studied. Many new materials have been synthesized. These non-oxides greatly enrich the iron-based correlated electronic systems and provide a fertile ground for the study of improper ferroelectrics. By adjusting the anions, lattice structures, electronic structures and magnetic properties can be well controlled.

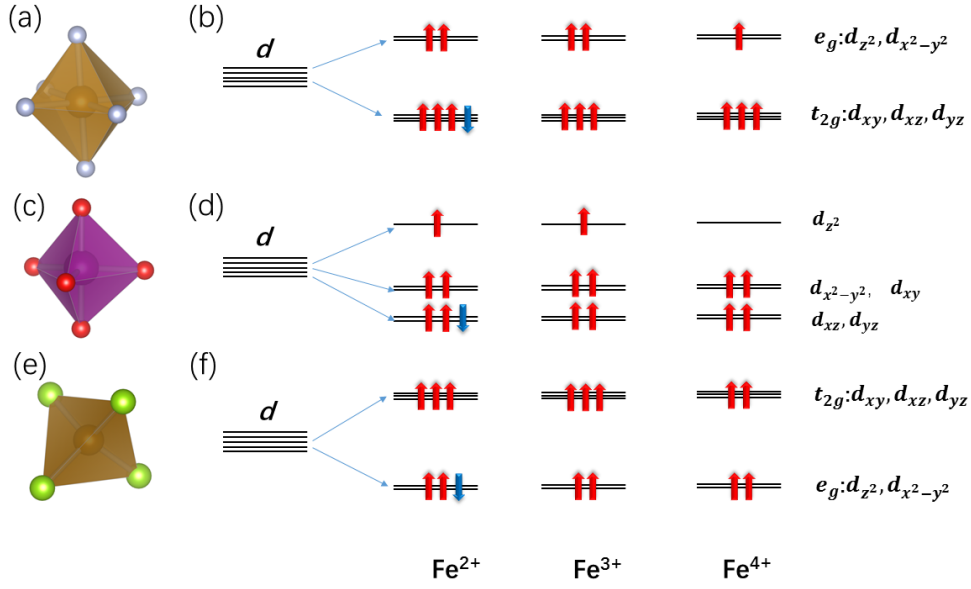


Figure 2. Typical crystal environments of iron and its corresponding crystal field splitting of 3d orbital. (a), (b) Octahedral crystal field; (c), (d) tetrahedral crystal field; (e), (f) tetrahedral crystal field. Spin up and spin down are represented by red and blue arrows, respectively.

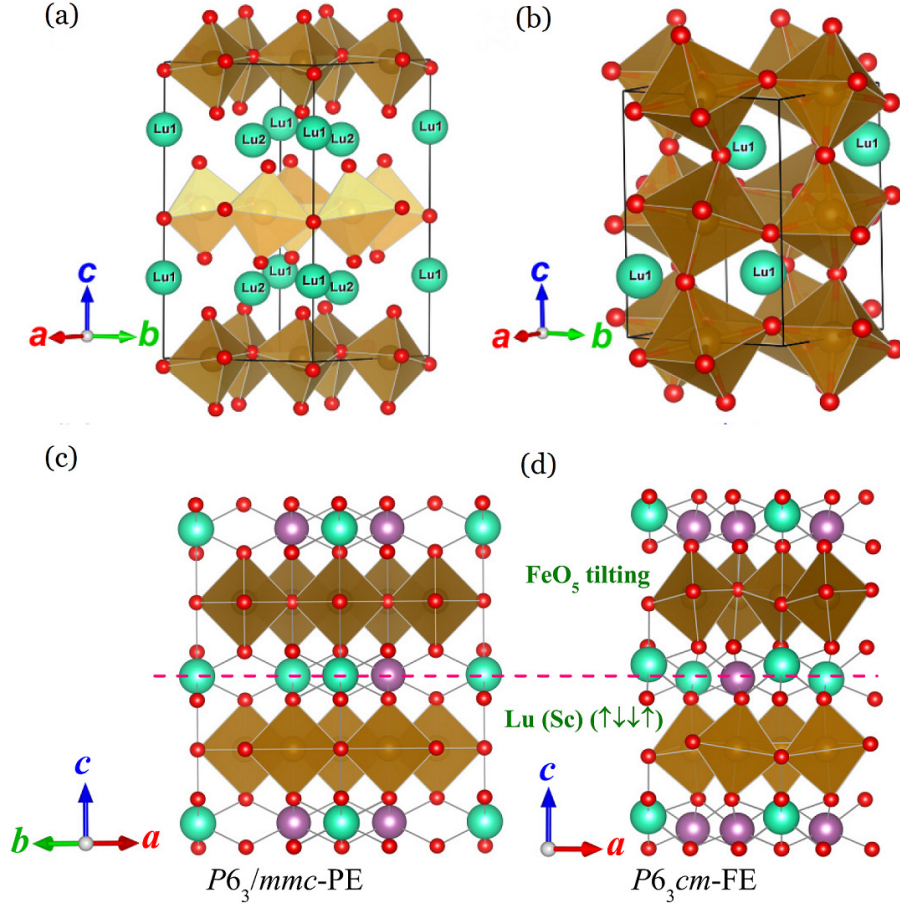


Figure 3. (a) Crystal structure of hexagonal LuFeO₃. In *h*-LuFeO₃, each Fe³⁺ are surrounded by five O, forming FeO₅ trigonal bipyramid. (b) Crystal structure of orthorhombic LuFeO₃. In *O*-LuFeO₃, each Fe³⁺ are surrounded by O₆ octahedral. The crystal structure of (c) paraelectric and (d) ferroelectric states of *h*-Lu_{0.5}Sc_{0.5}FeO₃. Reprinted figure with permission from [30] Copyright 2016 by the American Physical Society.

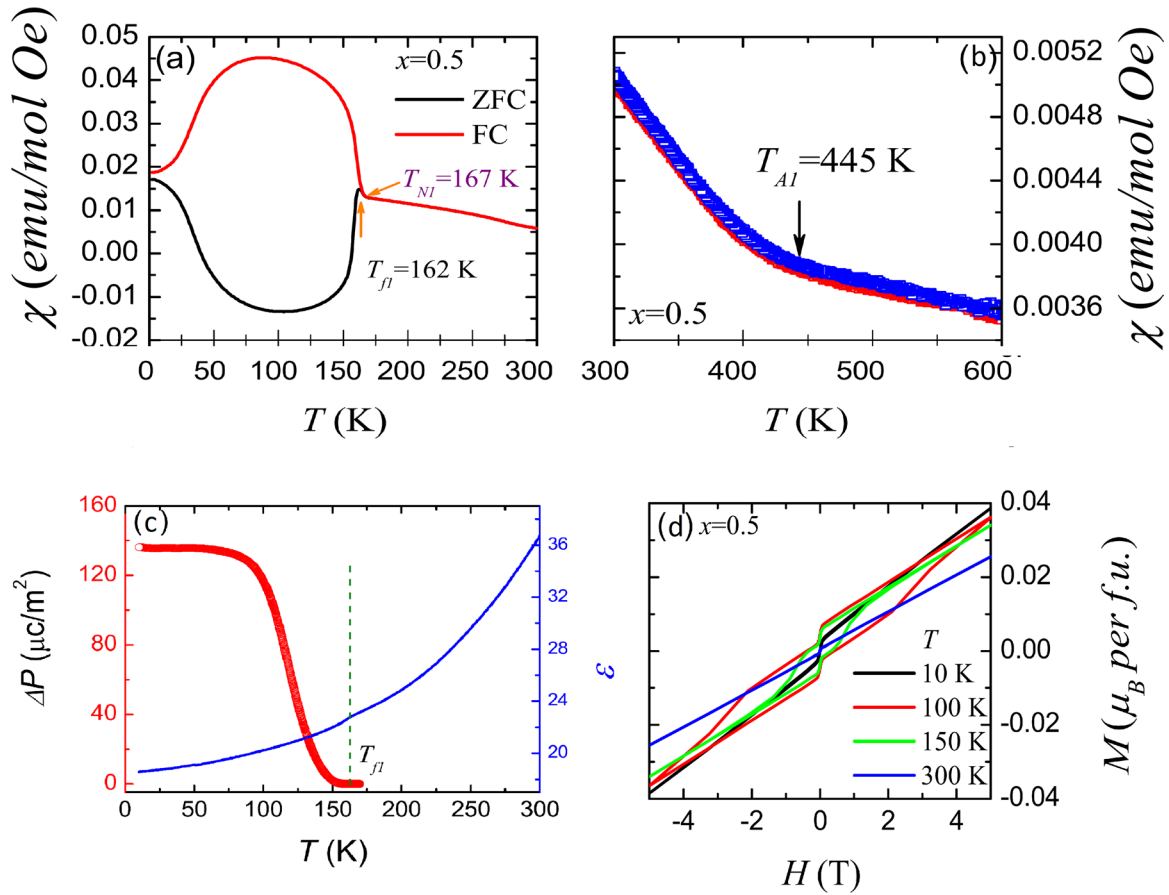


Figure 4. (a) Temperature dependence of magnetic susceptibility χ of sample $\text{Lu}_{1-x}\text{Sc}_x\text{FeO}_3$ $x = 0.5$ under zero field cooling (ZFC) and field cooling (FC) modes. (b) The high-temperature $\chi(T)$ data of sample $x = 0.5$ under ZFC and FC modes. (c) Temperature dependence of the evaluated polarization ΔP and dielectric constant (ϵ). (d) $M-H$ loops measured at temperature $T = 10, 100, 150$, and 300 K for sample $x = 0.5$. Reprinted figure with permission from [30], Copyright 2016 by the American Physical Society.

2. Iron-based multiferroics with improper ferroelectricity

In the following, we will introduce several recently reported iron-based multiferroics with different magnetoelectric mechanisms. Although in all these compounds the element iron plays as the common leading role, these multiferroics cover almost all types of improper ferroelectricity, including geometric ferroelectricity, magnetic ferroelectricity, electronic ferroelectricity.

2.1. Hexagonal LuFeO_3 : geometric ferroelectricity

Geometric ferroelectricity come from the structural instability in ionic crystals, similar to the conventional proper ferroelectricity. However, the driving forces are distinguishable between these two types of ferroelectricity. In proper ferroelectrics like BaTiO_3 , the polar phonon mode, i.e. the displacement of Ti^{4+} , is driven by forming a coordination bond between Ti^{4+} and one of its neighbor O anions. The empty $3d$ orbital of Ti is crucial for this formation of coordination bond, implying the well-known d^0 rule for proper ferroelectricity [23]. In contrast, in geometric ferroelectrics like hexagonal YMnO_3 , the condensation of several non-polar phonon modes, i.e. trimerization of Mn triangles and tiltings

of oxygen hexahedra, drives an uncompensated displacement of Y^{3+} although neither Y^{3+} nor Mn^{3+} themselves is ferroelectric active [12]. In other words, such improper ferroelectricity from geometric frustration, does not rely on the re-hybridization and covalency between ferroelectric-active cations and anions. Therefore, the geometric polar structure can be rather robust against carrier doping, and may persist even in the metallic materials [24].

Hexagonal RMnO_3 's (R : rare earth or Y) usually have high ferroelectric transition temperatures ($T_C \sim 1000$ K), however, their AFM Néel temperatures (T_N 's) only ~ 100 K [25]. The low magnetization temperature, as well as its large divergence with T_C , prohibit strong magnetoelectric coupling and the application at ambient condition. As an alternative family, hexagonal RFeO_3 's also own geometric ferroelectricity, due to the same mechanism. It is expectable that stronger $\text{Fe}^{3+}-\text{Fe}^{3+}$ exchange interaction may enhance the magnetic ordering temperatures.

RFeO_3 can crystallize in both the orthorhombic ($o\text{-RFeO}_3$) structure and hexagonal ($h\text{-RFeO}_3$) structure, while the orthorhombic one is the stablest at ambient condition. Taking the LuFeO_3 for example, its orthorhombic structure with the space group $Pbnm$ is non-polar (as shown in figure 3(b)) and exhibits C-type antiferromagnetism below 620 K [26]. In contrast, a polar structure (space group $P6_3cm$, as shown in

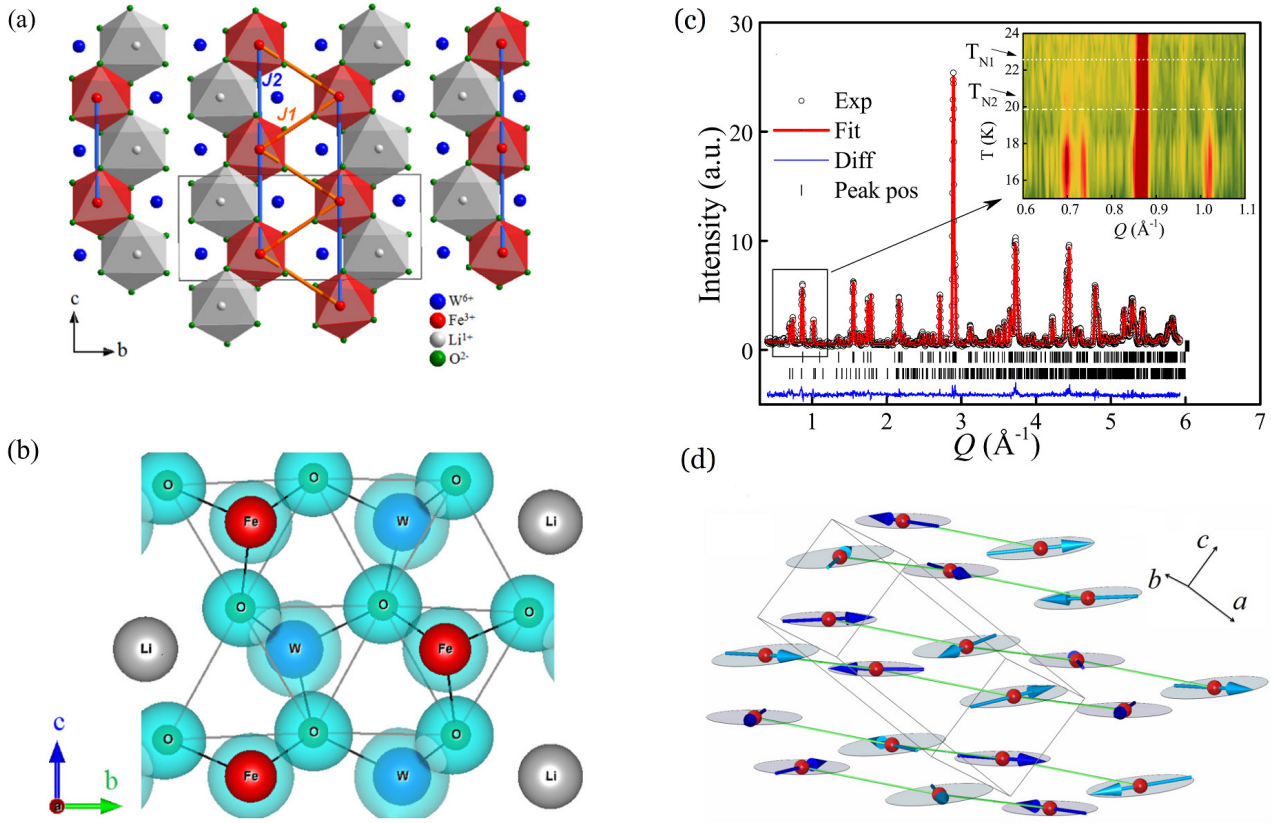


Figure 5. (a) The crystal structure of $\text{LiFe(WO}_4)_2$, projected in the bc plane. Blue: W; green: O; gray: Li; red: Fe. (b) Contour plot of charge density derived from density functional theory results with noncollinear magnetic state, $k = (1, 0, 1/3)$. The nearest neighbor Fe–O, W–O, and O–O are connected. (c) The neutron powder diffraction pattern measured at 5 K and corresponding Rietveld fit. Inset: contour plot of the temperature dependence of magnetic Bragg peaks at small momentum transfer Q . (d) The sketch of noncollinear magnetic order fitted from the neutron powder diffraction data. The moments of Fe form a cycloidal structure with iron magnetic moments nearly confined to the plane defined by the k vector and $[010]$ direction. The cycloid rolls along the solid green lines. The moments at the two Fe positions related by the twofold axis symmetry, Fe1 ($0, y, 1/4$), Fe2 ($0, -y, 3/4$), are depicted by different colors. Reprinted figure with permission from [53], Copyright 2017 by the American Physical Society.

figure 3(a) has also been found in bulk (meta-stable) and thin films [27]. In this hexagonal phase, the paraelectric (space group $P6_3/mmc$) to ferroelectric transition at ~ 1050 K can be achieved via the freezing of three phonon modes Γ_2^- , K_1 , and K_3 as shown in figures 3(c)–(d) [12]. Distinct with the well-recognized ferroelectricity, the magnetism of $h\text{-LuFeO}_3$ was under debate. First, Wang *et al* reported an AFM order below 440 K, followed by a spin reorientation resulting in a weak ferromagnetic order below 130 K on $h\text{-LuFeO}_3$ thin film [28]. However, a latter work by Disseler *et al* could not confirm the high-temperature antiferromagnetism, while only the low-temperature transition at $\sim 115\text{--}155$ K was reported [29].

The metastability of bulk $h\text{-LuFeO}_3$ phase makes the comprehensive study of its magnetism quite challenging. Recently, several groups reported that a stable hexagonal structure can be achieved in scandium (Sc)-substituted LuFeO_3 . At the half-substituted compounds $(\text{Lu}_{0.5}\text{Sc}_{0.5})\text{FeO}_3$, pure hexagonal bulk phase can be synthesized [31, 32]. Both the Mössbauer spectrum and x-ray photoelectron spectroscopy (XPS) results suggest that the Fe ion exists as Fe^{3+} in this composition. First-principles calculations show that the hexagonal structure can be stabilized by partial Sc substitution, while the multiferroic properties, including the noncollinear magnetic order and geometric ferroelectricity, remain robustly unaffected [30].

Therefore, $\text{Lu}_{1-x}\text{Sc}_x\text{FeO}_3$ can act as an alternative material to check the multiferroicity of LuFeO_3 and related materials in the bulk form.

Magnetic susceptibility (χ) for the $x = 0.5$ sample does show a magnetic transition temperature $T_N \sim 167$ K at which ZFC and FC curves split, followed by a weak anomaly at $T_f \sim 162$ K at which ZFC curve peaks as shown in figure 4(a). Usually, these two temperatures should be identical, indicating the magnetic transition. However, due to the intrinsic quenching disorder caused by Sc substitution, there is a small difference (5 K) in this system. Regarding the conflict of magnetism above room temperature in $h\text{-LuFeO}_3$ film, magnetic measurement on bulk samples shows a magnetic anomaly $\sim T_A = 445$ K as shown in figure 4(b), which needs further study to figure out its origin. Magnetic hysteresis loop ($M - H$) (figure 4(d)) suggests a weak ferromagnetic signal below T_A , which is possibly the spin-canting moment from the AFM background as proposed by Wang *et al*. Once the AFM order is established, the weak ferromagnetic canting can be driven by the Dzyaloshinskii–Moriya interaction.

For the ferroelectric properties, $(\text{Lu}_{0.5}\text{Sc}_{0.5})\text{FeO}_3$ are already ferroelectric at room temperature, which is driven by the freezing of the three collective phonon modes (Γ_2^- , K_1 , K_3). Further dielectric constant shows a weak anomaly around

T_f as shown in figure 4(c). This additional ferroelectric transition was thought to originate from spin reorientation, which should be magnetoelectrically active. The saturated polarization can reach $\sim 135 \mu\text{C m}^{-2}$ below 80 K for polycrystalline samples. This direct pyroelectric polarization signal around magnetic transitions, which is a fingerprint of magnetoelectricity, is first observed among hexagonal RMnO_3 and RFeO_3 series.

2.2. $\text{LiFe}(\text{WO}_4)_2$: cycloidal spins driving ferroelectricity

As aforementioned, the weak magnetoelectric coupling in multiferroics with proper ferroelectricity is an intrinsic drawback, which is difficult to overcome. Even in aforementioned geometric improper ferroelectrics, the independent origins of magnetism and ferroelectricity prohibit intrinsically strong magnetoelectricity. To realize strong magnetoelectric coupling and reliable magnetic/ferroelectric mutual regulation, one possible solution is the so-called type-II multiferroic family, in which their ferroelectricity is generated by some special spin orders. Since the ferroelectricity is a result of spin texture, changing the spin configurations (such as by applying magnetic field or other stimulations) can modulate ferroelectricity.

To obtain the type-II multiferroics, the special spin orders should break the spatial inversion symmetry, as required by the ferroelectricity. An effective approach is to stabilize cycloidal spin orders with helicity, i.e. clockwise and anti-clockwise. The first mostly studied system is orthorhombic TbMnO_3 , in which the bc -plane spiral spin order forms below 28 K. Such a spiral spin order generates a polarization pointing to the c -axis. This polarization can be switched from the c -axis to a -axis by magnetic field applied along the b -axis, rendering the strong magnetic-control of polarization [10, 33]. The counter-effect, i.e. electric-control of magnetism, is more difficult to be observed, since here the magnetism is more fundamental than polarization in the type-II multiferroics. Even though, the tuning of magnetic helicity by an electric field has been observed [34], as an unambiguous evidence of electric-control of magnetism.

The underlying magnetoelectricity can be abstractly expressed as [35, 36]:

$$\mathbf{P}_{ij} \sim \mathbf{e}_{ij} \times (\mathbf{S}_i \times \mathbf{S}_j), \quad (2)$$

where \mathbf{S} denote spins and \mathbf{e}_{ij} is the direction vector from spin \mathbf{S}_i to spin \mathbf{S}_j . The driving force for this type of magnetoelectricity is the Dzyaloshinskii–Moriya interaction. This equation is valid for lots of multiferroics in this catalog [37].

In fact, a large portion of spiral-spin multiferroics are Mn oxides, e.g. RMnO_3 [38–40], RMn_2O_5 [41–44], MnWO_4 [45, 46], and $\text{CaMn}_7\text{O}_{12}$ [47–49]. Besides these Mn oxides, others transition metal oxides are also available, as spiral-spin multiferroics, e.g. CuO [50], CoCr_2O_4 [51], $\text{Ni}_3\text{V}_2\text{O}_8$ [52]. Among these materials, MnWO_4 is a tungstate member with the wolframite structure, which also displays frustrated magnetic orders. More than ten years ago, MnWO_4 was already experimentally confirmed to be a multiferroic material in the temperature range between 7.6 K and 12.7 K,

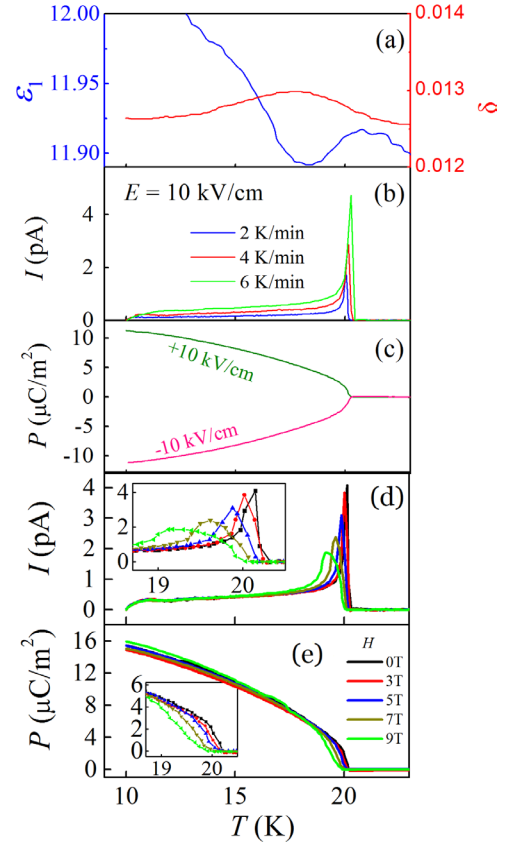


Figure 6. (a) Dielectric constant (left) and dielectric loss (right). (b) Pyroelectric currents measured with different warming rates. The poling electric field is 10 kV cm^{-1} . (c) Integrated pyroelectric polarization P 's with positive/negative poling fields. The peak position of dielectric constant coincides with the emergence of pyroelectric P 's. (d) Pyroelectric currents measured under different magnetic fields. (e) The corresponding pyroelectric P 's. Insets: magnified views around T_{N2} . Reprinted figure with permission from [53], Copyright 2017 by the American Physical Society.

corresponding to the incommensurate elliptical spiral phase [45, 46]. However, it is very strange that MnWO_4 is the sole multiferroic in the tungstate family for more than ten years, while in other families (e.g. RMnO_3) usually more than one multiferroic materials exist with similar magnetoelectric mechanism.

Very recently, some of the authors experimentally reported the second multiferroic tungstate $\text{LiFe}(\text{WO}_4)_2$, in which Li and Fe take place of Mn in MnWO_4 [53]. The crystal structure of $\text{LiFe}(\text{WO}_4)_2$ is described in the monoclinic space group $C2/c$. It consists of stacking (100) layers made of mixed $[\text{LiO}_6]$ and $[\text{FeO}_6]$ edge-sharing octahedra arranged in zigzag chains, separated by layers composed of tungstate $[\text{WO}_6]$ octahedra. The chain contains both Li and Fe octahedra alternating along the c direction. Such atomic arrangement leads to the doubling of the unit cell along the b direction, thus it stands for a sub-branch of tungstate: double tungstate. Figure 5(a) shows the crystal structure of $\text{LiFe}(\text{WO}_4)_2$.

The spin order of this double tungstate was investigated by neutron and magnetic susceptibility measurements. Curie–Weiss fitting yields a negative $\theta_{\text{CW}} = -69.5 \text{ K}$, suggesting strong AFM interactions between Fe^{3+} spins. An effective

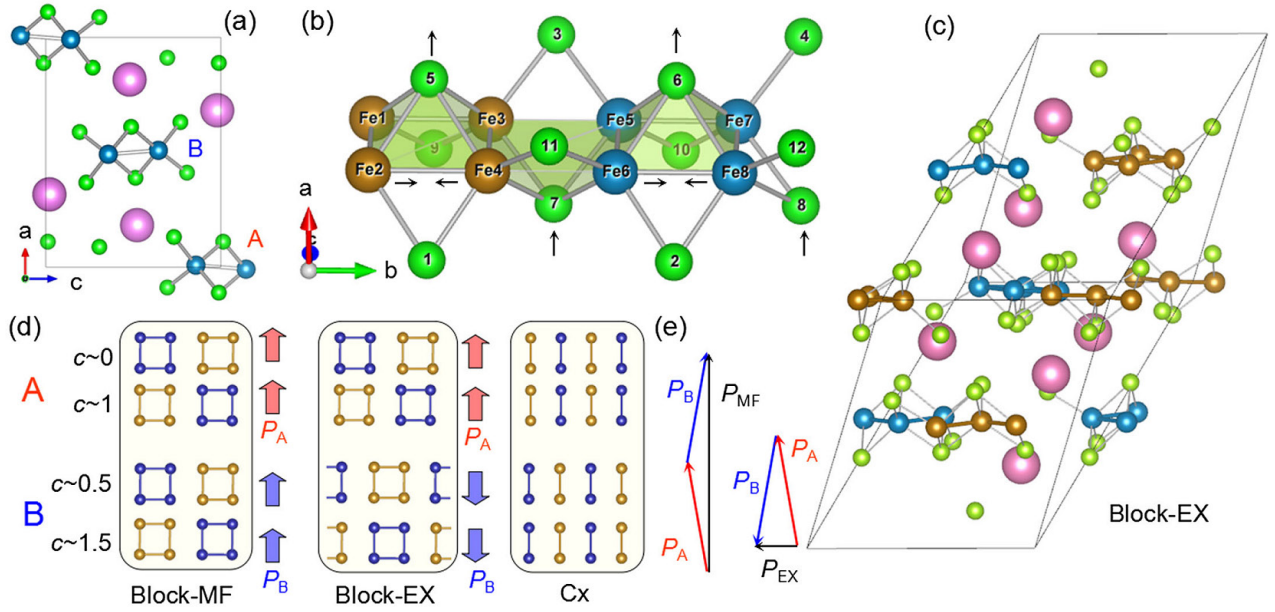


Figure 7. Crystal and magnetic structures of BaFe₂Se₃. (a) Side view along the *b* axis. Blue: Fe; green: Se; pink: Ba. (b) A Fe–Se ladder along the *b* axis and its magnetic order. Partial ionic displacements driven by the exchange striction are marked as black arrows. (c) A unit cell considering the AFM order. (d) Spin structures. Left: Block-MF (MF: multiferroic); middle: Block-EX (EX: experimental); right: Cx (C-type stripe along the *x* axis). The side arrows denote the local ferroelectric polarization of each ladder. In (b)–(d), the spins (\uparrow/\downarrow) of Fe's are distinguished by colors. (e) Vector addition of ferroelectric polarization's of ladders A and B. Reprinted figure with permission from [58], Copyright 2014 by the American Physical Society.

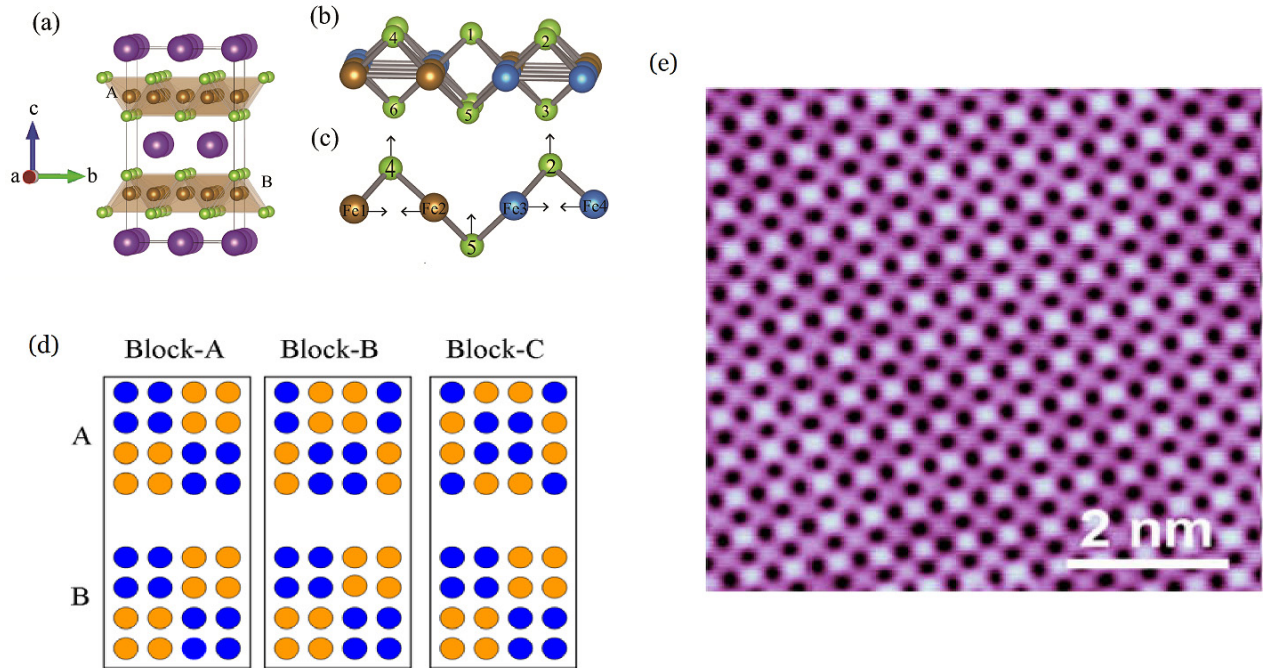


Figure 8. (a) Crystal structure of KFe₂Se₂. Purple: K; green: Se; brown: Fe. Two Fe sheets in a minimum unit cell are indicated as A and B. (b) One FeSe layer with magnetism. Brown: spin up; blue: spin down. (c) A side view of FeSe bonds. The ionic displacements driven by exchange striction are indicated by arrows. (d) Sketch of the block AFM series. A and B denote the two layers shown in (a). Left: Block-A. Middle: Block-B. Right: Block-C. Irons with spin up and spin down are distinguished by colors. [70] John Wiley & Sons. (e) The charge ordering in STM image of stoichiometric KFe₂Se₂. Reprinted figure with permission from [69], Copyright 2012 by the American Physical Society.

paramagnetic moment of $6.075 \mu_B$ per Fe is found, which is very close to the expected value of effective moment ($5.92 \mu_B$) for high-spin Fe³⁺ ($S_z = 5/2$, $L = 0$). Neutron diffraction results suggest a short range magnetic ordering at 22.6

K and a long range spin order forms below 19.7 K as shown in figure 5(c). The refined magnetic structure of LiFe(WO₄)₂ is shown in figure 5(d). The magnetic moments of Fe form a cycloidal magnetic structure with the spins confined to the

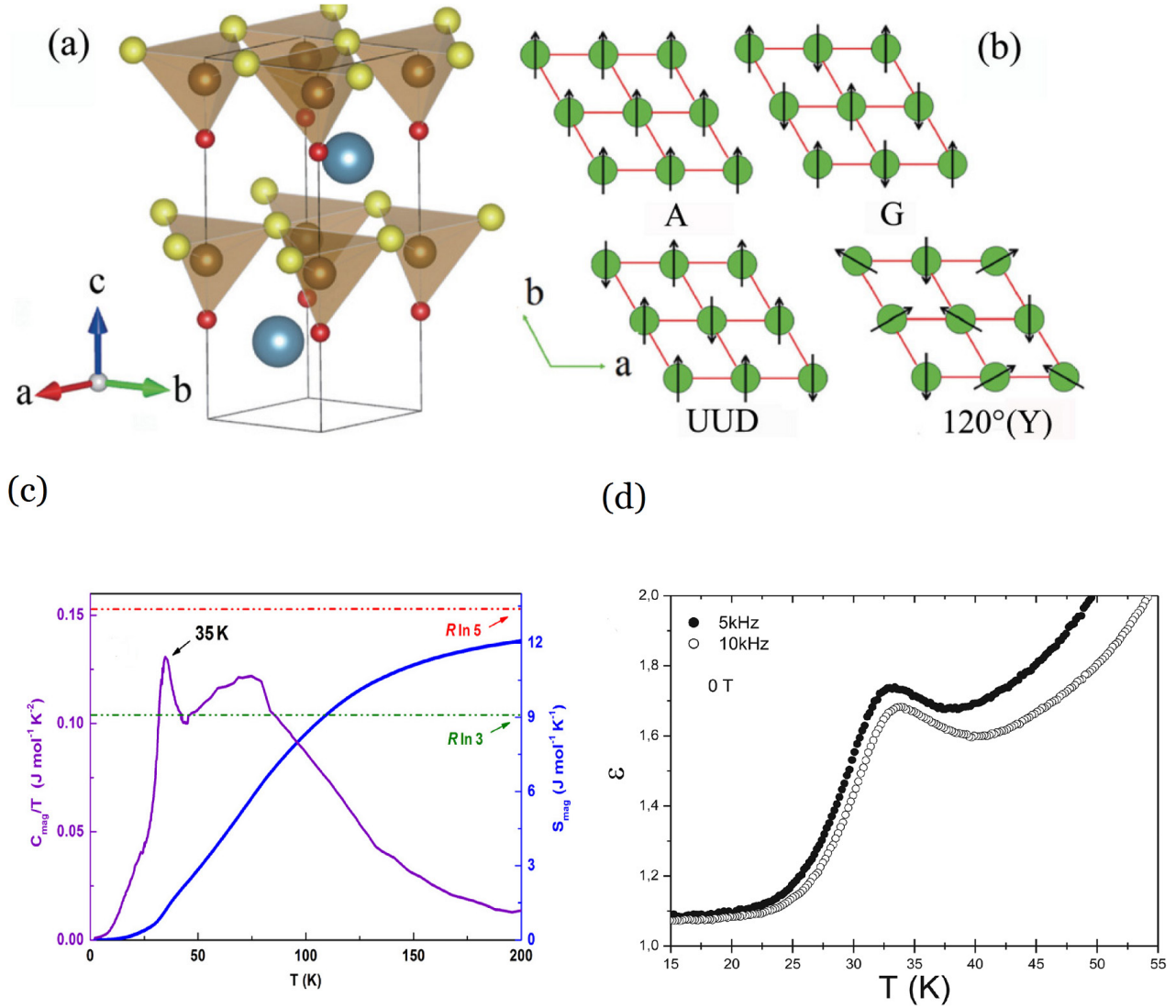


Figure 9. (a) Schematic crystal structure of CaOFeS. Blue: Ca; red: O; yellow: S; brown: Fe. (b) Sketch of possible spin configurations (denoted by arrows) in a two-dimensional triangular lattice. Between layers, both the parallel and antiparallel configurations have been calculated. Reprinted figure with permission from [77], Copyright 2017 by the American Physical Society. (c) Temperature dependence of magnetic entropy and C_{mag}/T for CaOFeS. Reprinted figure with permission from [75], Copyright 2015 by the American Physical Society. (d) Thermal dependence of the dielectric permittivity ϵ (measuring frequency $f = 5$ and 10 kHz). Reprinted with permission from [76]. Copyright 2015 American Chemical Society.

plane defined by the k vector and $[010]$ direction. The envelope of the cycloid is nearly circular, with a refined amplitude of the magnetic moment of $4.2 \mu_B$. The spin ordering temperature is remarkably enhanced with that in MnWO_4 (12.7 K). This enhancement is very precious, considering the fact that each $[\text{FeO}_6]$'s are separated by $[\text{WO}_6]$'s and $[\text{LiO}_6]$'s. Thus, the exchanges between Fe spins are not more indirect than those between Mn spins in $\text{Mn}(\text{WO}_4)_2$. Further density function theory calculations confirmed that the cycloidal magnetic structure as the possible ground state and revealed that the magnetic coupling between Fe^{3+} ions can be mediated via Fe–O–O–Fe and Fe–O–W–O–Fe as shown in figure 5(b). Such complicated exchange routes suppress the effective strength of magnetic couplings. Even though, thanks to the intrinsically stronger superexchange between Fe^{3+} – Fe^{3+} than Mn^{2+} – Mn^{2+} , the magnetic Néel temperature remains improved.

As mentioned before, this proposed cycloidal magnetic structure can break the spatial inversion symmetry and lead to the magnetic ferroelectricity. Dielectric constant $\epsilon(T)$ measured at 1 kHz (figure 6(a), left axis) does show a broad peak around $T_{\text{N}2}$, which is an indication of ferroelectricity below this temperature. Pyroelectric curves ($I_{\text{pyro}} - T$) with three warming rates (2, 4, and 6 K min^{-1}) show peaks at $T_{\text{N}2}$ without any shift (figure 6(b)). Integrated polarization $P(T)$ curves based on positive and negative pooling electrical $I_{\text{pyro}} - T$ curves are shown in figure 6(c). The symmetrical $P(T)$ curves upon the positive/negative poling fields suggest the reversibility of polarization. According to $P(T)$ and $\epsilon(T)$, the ferroelectricity emerges just below $T_{\text{N}2}$. This is a strong evidence for magnetism driven ferroelectricity. Therefore, an intrinsic magnetoelectricity should be expected. $I_{\text{pyro}} - T$ curves and corresponding $P(T)$ curves are measured under different magnetic fields as shown in figures 6(d)–(e) with increasing

magnetic field. Peaks at T_{N2} in both curves shifts to lower temperatures and becomes weaker and broader, implying the magnetoelectric coupling between magnetic order and dipole order. Density functional calculation also confirmed the cycloidal spin order driving ferroelectricity, and the estimated polarization was $24.5 \mu\text{C m}^{-2}$, in agreement with the experimental pyroelectric polarization ($\sim 12 \mu\text{C m}^{-2}$ for polycrystalline sample) qualitatively.

Finally, it should be noted that there is a related compound $\text{NaFe(WO}_4)_2$, which also shows noncollinear spin order. However, it was found non-ferroelectric and its concrete positions of Na and Fe are different from Li and Fe in $\text{LiFe(WO}_4)_2$ [54].

2.3. Iron selenides: exchange striction driving ferroelectricity

Besides cycloidal spin order, some collinear spin order, e.g. $++--$ type, can also break spatial reversal symmetry for particular crystalline structures. The first material in this catalog was orthorhombic $\text{HoMnO}_3/\text{YMnO}_3$ as proposed by Sergienko, Şen and Dagotto, which owns the zigzag E-type antiferromagnetism [55]. Another early member is $\text{Ca}_3\text{CoMnO}_6$ with quasi-one-dimensional magnetic chains [56]. Although these materials also belong to type-II multiferroics, the underlying magnetoelectric mechanism is rather different from the above cycloidal spin driven one. Generally speaking, the cycloidal ones need the relativistic spin-orbit coupling to generate the polarizations, and thus the polarizations are usually very weak considering the strength of spin-orbit coupling of most transition metal ions. In contrast, the driving force in $\text{HoMnO}_3/\text{YMnO}_3$ and $\text{Ca}_3\text{CoMnO}_6$ is the so-called exchange striction, which can be abstractly described as $J\mathbf{S}_i \cdot \mathbf{S}_j$, where J is the exchange coefficient. Since in most materials the exchange is much stronger than the Dzyaloshinskii–Moriya interaction, the induced polarization can be much larger than the cycloidal spin order induced one, e.g. up to $\sim 1 \mu\text{C cm}^{-2}$ in orthorhombic YMnO_3 [55, 57]. However, the multiferroic temperatures remain low in most materials in this catalog.

2.3.1. BaFe_2Se_3 . This exchange striction mechanism can also work in non-oxides. For example, iron-selenide BaFe_2Se_3 was predicted by some of the authors to be a type-II multiferroic, whose polarization is driven by exchange striction [58]. This work not only finds a new multiferroic material, but also connect the multiferroics with the superconductor family, since BaFe_2Se_3 is a member of the iron-based superconductor family.

BaFe_2Se_3 forms an orthorhombic structure. Each unit cell has two iron ladders (labeled A and B), built by edge-sharing FeSe_4 tetrahedra, as shown in figure 7(a). Long-range AFM order is established below 256 K. Both neutron studies and first principles calculations reported an exotic block AFM order [59–62]. The Hartree–Fock approximation to the five-orbital Hubbard model also confirmed the stability of the block AFM phase and revealed other competing phases, e.g. the Cx phase [63].

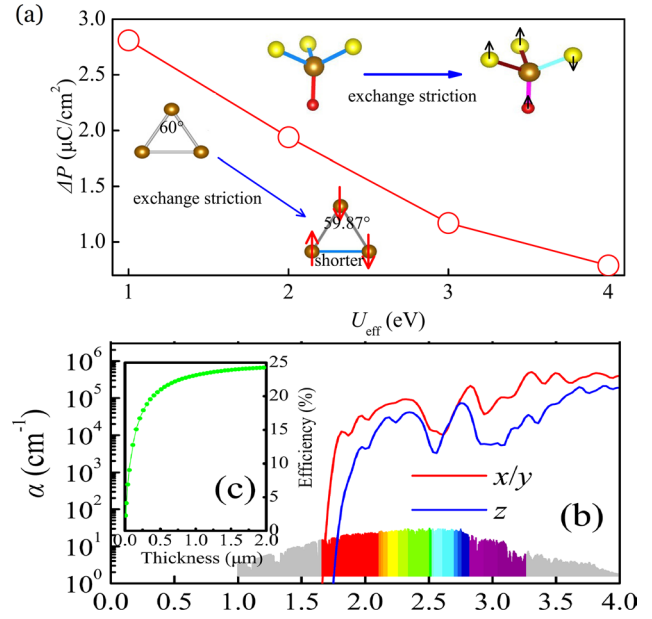


Figure 10. (a) The magnetoelectricity, i.e. change of polarization upon G-AFM ordering. (b) The calculated absorption coefficient $\alpha(\omega)$ of CaOFeS . The energy spectrum of solar light is shown for reference. (c) Calculated maximum photovoltaic energy conversion efficiency for CaOFeS as a function of absorber layer thickness. Reprinted figure with permission from [77], Copyright 2017 by the American Physical Society.

The block AFM order is particularly interesting because it breaks parity symmetry and displays exchange striction effects. Neutron measurements revealed that the nearest-neighbor (NN) distances between $\text{Fe}(\uparrow)$ and $\text{Fe}(\uparrow)$ (or $\text{Fe}(\downarrow)$ and $\text{Fe}(\downarrow)$) at 200 K become 2.593 \AA , much shorter than the $\text{Fe}(\uparrow)$ – $\text{Fe}(\downarrow)$ distance 2.840 \AA [59]. However, such in-ladder striction between irons will not generate polarization. The polarization comes from the displacements of Se's.

As shown in figure 7(b), Se(5) is above the ladder's plane, while the next Se(7) is below, and the distances of Se(5) and Se(7) to the iron ladder plane should be the same in magnitude and opposite sign ('antisymmetric'). However, this antisymmetric could be broken by the block AFM order. The blocks made of four $\text{Fe}(\uparrow)$'s (or four $\text{Fe}(\downarrow)$'s) are no longer identical to blocks made of two $\text{Fe}(\uparrow)$'s and two $\text{Fe}(\downarrow)$'s [58, 64]. Then, the Se(5) and Se(7) heights do not need to be antisymmetric anymore; their distances to the ladder planes can become different. The same mechanism works for the edge Se's, e.g. Se(1) and Se(11). As a consequence, the atomic positions of Se break the space inversion symmetry, generating a local polarization pointing perpendicular to the iron ladders plane (almost along the a axis).

Theoretical analysis suggests that each ladder can be multiferroic. However, the net polarization is determined by how each ladder interacts with others. Neutron studies by Caron *et al* found the block AFM pattern shows a $\pi/2$ -phase shift between the NN A–B ladders but a π -phase shift between the NN A–A ladders (and NN B–B ladders), i.e. Block-EX state as shown in figure 7(d) [59, 65]. The shift between A–A ladders (or B–B ladders) will not change the direction of the induced local polarization, but the $\pi/2$ -phase shift between

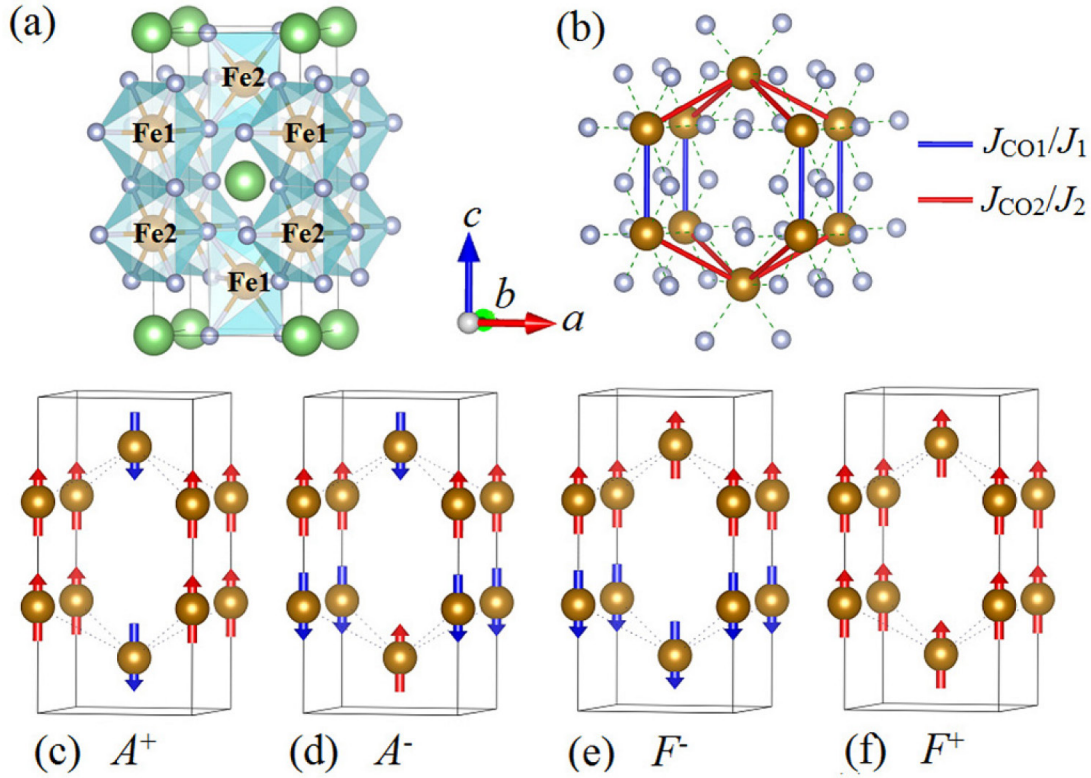


Figure 11. (a) Crystal structure of LiFe_2F_6 . Brown: Fe; green: Li; silver: F. HSS: $\text{Fe1} = \text{Fe2}$. LSS: $\text{Fe} \neq \text{Fe2}$. (b) The framework of Fe-F ions and the charge/magnetic exchange paths for J_{CO1}/J_1 and J_{CO2}/J_2 . (c)–(f) Sketch of different magnetic orders of Fe spins. F and A (+ and –) stand for ferromagnetic and AFM coupling between next-nearest neighbor (nearest neighbor) moments, respectively. Reprinted figure with permission from [92], Copyright 2017 by the American Physical Society.

A–B ladders will induce (nearly) opposite local polarization. A fully cancellation can be avoided due to the small canting angles between ladder A and B, leading to a net polarization along c axis as shown in figure 7(e).

According to the density functional theory calculation, the Block-EX state are found to be ferrielectric with a net polarization $\sim 0.19 \mu\text{C cm}^{-2}$ pointing mostly along c axis. The net polarization can be flipped if an external electric field is applied along c axis. If a large enough field is applied along the a axis, the ferrielectric (Block-EX) to FE (Block-MF) phase transition will occur, producing a 90° flipping and enhancement of polarization. The ferroelectric polarization of Block-MF state can reach $2 \mu\text{C cm}^{-2}$. Moreover, the 180° flipping of polarization can also be obtained by reversing the tilting angle between the planes of ladders A and B, without shifting the magnetic blocks [58].

However, due to the nonstoichiometry of BaFe_2Se_3 and thus low resistivity, the direct measurement of polarization becomes difficult. Even though, following neutron scattering already confirmed the polar structure [66]. And using high-resolution transmission electron microscope, Tian *et al* observed the local dipoles of each iron ladder (private communication).

2.3.2. KFe_2Se_2 . Besides the 123-type iron-selenide BaFe_2Se_3 , stoichiometric KFe_2Se_2 also show the block-type antiferromagnetism, which is not common in iron-based superconductors. KFe_2Se_2 forms the tetragonal crystal structure, whose space group is $I4/mmm$ (No. 139). In each unit

cell, there are two Fe layers, each of which is built by edge-sharing FeSe_4 tetrahedra. K ions intercalate between Fe–Se layers as shown in figure 8(a).

The block-type antiferromagnetism was first predicted by Li *et al* according to the density functional theory calculation [67], then its associated structural tetramerization was experimental revealed in KFe_2Se_2 thin film using scanning tunnelling microscope (STM) measurement by Xue's group [68, 69](figure 8(e)). The tetramerization of irons is driven by its block-AFM ordering. The NN distance between $\text{Fe}(\uparrow)$ and $\text{Fe}(\uparrow)$ (or $\text{Fe}(\downarrow)$ – $\text{Fe}(\downarrow)$) is shorten comparing with the one between $\text{Fe}(\uparrow)$ – $\text{Fe}(\downarrow)$, similar to the situation in BaFe_2Se_3 . Se(4) and Se(5) are located in the opposite sides of iron layer, as shown in figure 8(b). Originally, the distance of Se(4) and Se(5) to the iron layer should be identical. Due to the tetramerization, the shrunk $\text{Fe}(\uparrow)$ blocks will push Se(4) ion upward, while Se(5) will be lifted up due to the elongation of $\text{Fe}(\uparrow) - \text{Fe}(\downarrow)$ bond as shown in figure 8(c). Similar movements occur for other Se ions. As a result, the movements of Se ions break the inversion symmetry and generate a local dipole moment pointing perpendicular to the iron plane, i.e. along the c -axis [70].

Each Fe–Se layer should be multiferroic, this layered system can be either a ferroelectric one with a finite macroscopic ferroelectric polarization or an antiferroelectric one with canceled polarization, depending on the stacking of magnetic blocks along the c -axis. As shown in figure 8(d), there are three possible block-AFM order. The magnetic + lattice

space group changes from No. 139 ($I4/mmm$) to No. 51 ($Pmma$ for Block-A) or No. 36 ($Cmc2_1$ for Block-B) or No. 123 ($P4/mmm$ for Block-C), among which only the $Cmc2_1$ for Block-B is a polar space group. Density functional theory calculation performed by Zhang *et al* observed the difference in the bond lengths between $\text{Fe}(\uparrow)\text{--Fe}(\uparrow)$ (or $\text{Fe}(\downarrow)\text{--Fe}(\downarrow)$) and $\text{Fe}(\uparrow)\text{--Fe}(\downarrow)$, e.g. 2.542 Å and 2.929 Å, respectively [70]. Due to exchange striction, the heights of Se (to the iron plane) become different: 1.53 Å for Se(4) and 1.58 Å for Se(5), respectively. The net polarization calculated using the standard Berry phase method for block B is along the c -axis with magnitude increases from 0.48–2.1 $\mu\text{C cm}^{-2}$ depending on the choice of U in calculation [70]. For Block-A and Block-C, the dipole moments between any nearest-neighbor layers are aligned antiparallely, rendering the antiferroelectric fact.

According to the calculation, the block AFM series always own lower energies than other type of magnetic order, such as ferromagnetic, A-, C-, or G-type AFM states. Among the three types of block AFM, the ferroelectric Block-B owns the lowest energy at small effective U , while the antiferroelectric Block-C take places with increasing effective U . More importantly, the energy differences within the block AFM series are very tiny. Therefore, antiferroelectric-ferroelectric transition is possible via proper stimulates in this material.

2.3.3. CaOFeS . Besides aforementioned 123 and 122 iron selenides, the so-called 1111 series of iron oxysulfides can also be magnetoelectric. Usually, the 1111 series of iron pnictides, e.g. LaOFeAs , own a layered Fe square lattice, which undergoes a tetragonal-to-orthorhombic structural transition followed by the stripe AFM transition [71, 72]. However, here the 1111-type iron oxysulfide CaOFeS forms a layered triangular lattice [73–76]. As sketched in figure 9(a), it owns a hexagonal structure, whose space group is $P6_3mc$ (No. 186). In each unit cell, there are two ab -plane Fe layers, which are built by triangles of O--Fe--S_3 tetrahedra. Ca ions intercalate between S and O layers. This triangular lattice may provide the geometry for magnetic frustration. As shown in figure 9(b), if the spin is for Heisenberg type, a typical Y-type ground state usually appears with nearest-neighbor spins arranged with 120° in the two-dimensional triangular lattice. While if the spin is for Ising type, spins arranged in a two-dimensional triangular lattice can also form some exotic patterns. Neutron measurement performed by Jin *et al* found a partially ordered G-type Ising type AFM with a propagation vector of $k = (1/2, 1/2, 0)$ and an ordered magnetic moment of 2.59(3) μ_B/Fe along c at 6 K [75].

Dielectric measurements performed by Delacotte *et al* revealed the existence of a magnetodielectric effect near 33 K as shown in figure 9(d), which is in good agreement with the Néel temperature 35 K (figure 9(c)) [76]. Calculation performed by Zhang *et al* confirmed the G-type AFM (G-AFM) ground state and explained the mechanism of this magnetodielectric effect [77].

The crystalline structure of CaOFeS , with a space group $P6_3mc$ and point group 6mm, is polar, due to the unequivalence of O and S. But this polar structure is irreversible since the layers of O and S are fixed. The special G-AFM order

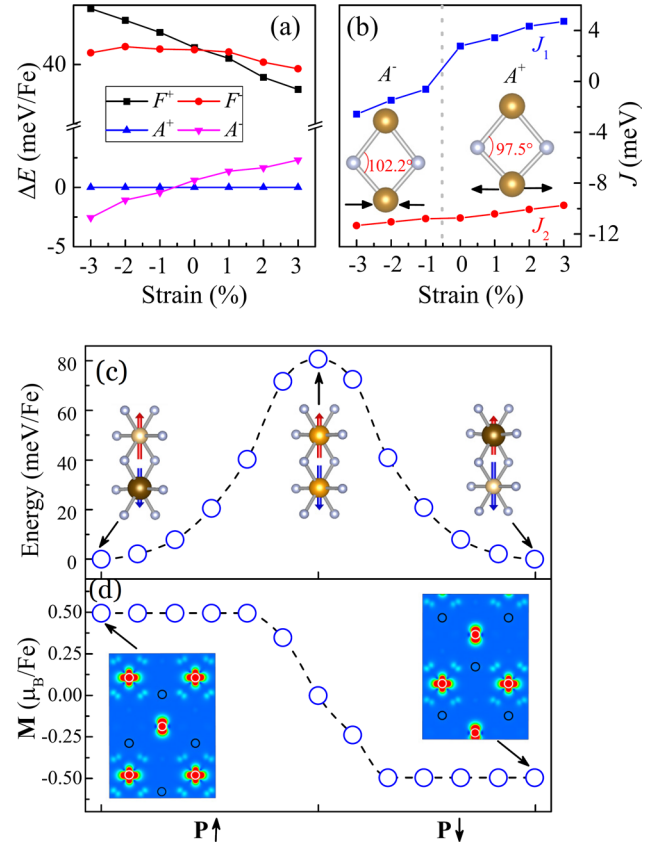


Figure 12. (a) Results for strained LiFe_2F_6 . (a) Energies of the F^+ , F^- , A^+ , and A^- states as a function of strain. The energy of A^+ state is the reference. (b) Strain dependent exchanges for the Heisenberg model. Insert: sketch of the bond angle of $\text{Fe}^{2+}\text{--F--Fe}^{3+}$ for the J_1 path. (c) Sketch of CO-mediated magnetoelectricity in strained (-3%) LiFe_2F_6 . (d) Switch of ferroelectric \mathbf{P} simulated by the NEB method. The simulated energy barrier for switching should be considered as the upper limit in the real experiment, while other paths/processes with lower barriers are possible. Insets: Initial, intermediate, and final structures. (b) The corresponding switch of magnetic \mathbf{M} obtained in the NEB process. Insets: The corresponding profiles (viewed from the $[110]$ direction) of the partial charge density for the topmost valence band. White/black circle: $\text{Fe}^{2+}/\text{Fe}^{3+}$. Reprinted figure with permission from [92], Copyright 2017 by the American Physical Society.

breaks the trigonal (i.e. 120° rotation) symmetry of the triangular lattice. In each Fe triangle, there are one $\text{Fe}(\uparrow)\text{--Fe}(\uparrow)$ (or $\text{Fe}(\downarrow)\text{--Fe}(\downarrow)$) bond and two $\text{Fe}(\uparrow)\text{--Fe}(\downarrow)$ bonds, which are no longer symmetric. This breaking of symmetry will distort the lattice, by shrinking the $\text{Fe}(\uparrow)\text{--Fe}(\downarrow)$ bonds but elongating others. According to the density functional theory optimized structure, such exchange striction will also result in the change of Fe–Fe distance up to 0.008 Å, i.e. the triangles are no longer regular but with 0.13 Å correction for $\angle_{\text{Fe--Fe--Fe}}$ as shown in figure 10(a) [77]. Such a tiny distortion is beyond the current experimental precision of structural measurement. The distortion of Fe–S bonds are more serious, reaching 0.069 Å as mentioned before. It is the displacements of S ions along the c axis responsible for the observed magnetodielectric effect.

Strictly speaking, CaOFeS review here is not a multiferroic since it is polar but not ferroelectric. However, it shows the

Table 1. Comparison of four improper ferroelectrics and their basic physical characteristics. ME: magnetoelectric.

	Geometric	Cycloidal spin	Exchange striction	Charge ordering
Material	LuFeO ₃	LiFe(WO ₄) ₂	BaFe ₂ Se ₃	LiFe ₂ F ₆
Ferroelectric T_C	~1050 K	~20 K	~256 K	~400 K
Magnetic T_N	~400/160 K	~23 K	~256 K	~100 K
ME Coupling	Spin-lattice	Spin-orbit	Spin-lattice	Spin-charge

magnetoelectric effect and underlying mechanism is common with some type-II multiferroics with exchanges striction.

In addition, theoretical studies predict a large coefficient of visible light absorption shown in figure 10(b). The maximum photovoltaic energy conversion is estimated to be ~24.2% [77]. Compared with the estimated efficiency of some other photovoltaic materials, e.g. AgInTe₂ (27.6%), CuBiS₂ (16%), CH₃NH₃PbI₃ (30%), and CuBiS₂ (22%) [78–80], this efficiency is still valuable. Considering that the polar effect will enhance the electron–hole separation which has not been take into account in this estimation, CaOFeS may be a potential photovoltaic material with prominent efficiency.

2.4. LiFe₂F₆: charge ordering driving ferroelectricity

The type-II multiferroics as we discussed in sections 2.2 and 2.3 have strong magnetoelectric coupling since their ferroelectricity directly originates from magnetism. However, in these materials, the magnetism M is a primary parameter, but the polarization P is not. Thus, it is easy to control P via magnetic field, but it is not easy to obtain the counter-effect. To overcome this drawback, the improper electronic ferroelectricity (or so-called charge ordering driving ferroelectricity) may provide a solution.

Iron-based compounds are naturally a candidate for charge ordering type multiferroics due to the multiple stable valence state of iron. For example, the first proposed multiferroics material generated by charge ordering, LuFe₂O₄, its ferroelectric is reported to be induced by a combination of the bilayer character of the crystal structure and the frustrated charge ordering in each layer [81–85]. Another example is Fe₃O₄. Fe₃O₄ becomes ferrimagnetic below 860 K, following by the famous Verwey transition at 120 K. It displays ferroelectricity below the Verwey temperature due to the charge ordering between Fe³⁺ and Fe²⁺ ions on B site that surrounded by oxygen octahedron [86]. However, there are drawbacks for both materials. The ferroelectricity mechanism of LuFe₂O₄ was questioned recently [87–89]. Fe₃O₄ is a narrow band insulator below Verwey temperature, resulting in leaking current in experimental demonstration [90, 91].

Recently, an iron-based fluoride LiFe₂F₆ was predicted to be a rare multiferroic with both large magnetization and polarization mediated by charge ordering [92]. The stronger electronegativity of F may reduce the hybridization between the 2p bands and 3d bands, leading to more insulating materials.

LiFe₂F₆ forms a tetragonal crystal structure (figure 11(a)). At high temperature, the high symmetric structure (HSS) without charge ordering is $P4_2/mnm$ (No. 136). Mössbauer spectrum measurement found the existence of Fe²⁺ and Fe³⁺ in LiFe₂F₆ above room temperature [93, 94]. Later, Fourquet

et al studied a LiFe₂F₆ single crystal using x-ray diffraction [94]. It revealed a low symmetric structure (LSS, No. 102, $P4_2nm$) for the charge ordering state. Even the charge ordering temperature is not fully determined, it is definitely above room temperature. Further, neutron powder diffraction revealed an A+ antiferromagnetism (figure 11(c)) below 105 K [95, 96].

On the basis of these experimental observations, Lin *et al* performed a theoretical study on the ferroelectric properties of this compound [92]. They demonstrate that LiFe₂F₆ is an AFM ferroelectric. The ferroelectricity are indeed induced by charge ordering. Thus, the charge order transition is also the nonpolar/polar transition. The dipole moment formed by the Fe²⁺–Fe³⁺ pair is estimated to be 12.4 $\mu\text{C cm}^{-2}$. More interestingly, calculation found that the energy of A-AFM state as shown in figure 11(d) with a net magnetization 0.5 μ_B/Fe is only slightly higher (0.5 meV/Fe) than that of the ground state A⁺. It can be achieved via compressive strain beyond –0.5%. It is expected to flip the net magnetization together with the polarization by an electric voltage as shown in figures 12(a) and (b), which avoids the drawback of magnetic ferroelectrics, provides the desired magnetoelectric function in practice.

3. Summary and perspective

In this topical review, the concept of improper ferroelectrics was introduced. Its mechanisms and advantages compared to proper ferroelectrics were also discussed. It is noticeable that the focused systems of improper ferroelectrics have shifted gradually from Mn-based compounds to iron-based compounds. Recent progresses on some typical iron-based improper ferroelectrics have been reviewed in this article, which covered all three types of improper ferroelectrics. Several typical materials are reviewed, which are briefly summarized in table 1. The first example is the hexagonal (Lu_{0.5}Sc_{0.5})FeO₃, which is a geometric ferroelectric material. Theoretical calculation confirms that the partial substitution of Lu by Sc can stabilize the hexagonal structure while its improper ferroelectricity is not affected. Direct pyroelectric polarization signal around the low temperature magnetic transitions is observed as a fingerprint of magnetoelectricity. The second example is LiFe(WO₄)₂, which is found to be the second multiferroic tungstate. Although the effective strength of magnetic coupling is suppressed by complicated indirect exchange routes, the magnetic Néel temperature remains improved compared to the first reported multiferroic tungstate Mn(WO₄)₂. The third family includes several iron selenides: BaFe₂Se₃, KFe₂Se₂, and CaOFeS, which display ferroelectricity or magnetodielectric effect due to exchange striction. The last example is LiFe₂F₆, which displays electric

ferroelectricity due to charge ordering. Its antiferromagnetism can be tuned to ferrimagnetism under moderate compressive strain. Furthermore, it is a candidate material to realize the electric control of magnetization.

As an emerging branch of multiferroics, the iron-based improper ferroelectrics still need extensive research before application. There are some drawbacks regarding their multiferroic performances. For example, the magnetic ordering temperatures are mostly below room temperature even though they have been improved compared to the corresponding isostructural Mn-based compounds. Furthermore, the magnetic orders in these compounds are typically AFM with nearly zero residue magnetization. To overcome these drawbacks, researchers need to find more candidate compounds with stronger exchange interactions and/or simpler exchange routes, and those iron-based compounds with ferrimagnetism.

Acknowledgment

We thank collaborators Q Z Huang, V O Garlea, T Zou, S D Shen, J Zhao, E Dagotto for their contributions in the works reviewed in this article. Work was supported by National Natural Science Foundation of China (Grant Nos. 11674055, 51721001, 11504048, and 11704109), National Key Research and Development Program of China (Grant No. 2016YFA0300101), and the Fundamental Research Funds for the Central Universities, China.

ORCID iDs

Jin Peng  <https://orcid.org/0000-0001-8863-2640>

Jun-Ming Liu  <https://orcid.org/0000-0001-8988-8429>

Shuai Dong  <https://orcid.org/0000-0002-6910-6319>

References

- [1] Schmid H 1994 *Ferroelectrics* **162** 317–38
- [2] Fiebig M 2005 *J. Phys. D: Appl. Phys.* **38** R123–52
- [3] Cheong S W and Mostovoy M 2007 *Nat. Mater.* **6** 13–20
- [4] Ramesh R and Spaldin N A 2007 *Nat. Mater.* **6** 21–9
- [5] Wang K F, Liu J M and Ren Z F 2009 *Adv. Phys.* **58** 321–448
- [6] Dong S, Liu J M, Cheong S W and Ren Z F 2015 *Adv. Phys.* **64** 519–626
- [7] Fiebig M, Lottermoser T, Meier D and Trassin M 2016 *Nat. Rev. Mater.* **1** 16046
- [8] Li Y, Jin Y, Lu X, Yang J C, Chu Y H, Huang F, Zhu J and Cheong S W 2017 *NPJ Quantum Mater.* **2** 43
- [9] Khomskii D 2009 *Physics* **2** 20
- [10] Kimura T, Goto T, Shintani H, Ishizaka K, Arima T and Tokura Y 2003 *Nature* **426** 55–8
- [11] Huang F T, Gao B, Kim J W, Luo X, Wang Y, Chu M W, Chang C K, Sheu H S and Cheong S W 2016 *NPJ Quantum Mater.* **1** 16017
- [12] van Aken B B, Palstra T T M, Filippetti A and Spaldin N A 2004 *Nat. Mater.* **3** 164–70
- [13] Pang H, Zhang F, Zeng M, Gao X, Qin M, Lu X, Gao J, Dai J and Li Q 2016 *NPJ Quantum Mater.* **1** 16015
- [14] Efremov D V, van den Brink J and Khomskii D I 2004 *Nat. Mater.* **3** 853
- [15] Wang J et al 2003 *Science* **299** 1719–22
- [16] Lee J H and Fishman R S 2015 *Phys. Rev. Lett.* **115** 207203
- [17] Tan H, Xu C, Li M, Wang S, Gu B L and Duan W 2016 *J. Phys.: Condens. Matter* **28** 126002
- [18] Xu C, Yang Y, Wang S, Duan W, Gu B and Bellaiche L 2014 *Phys. Rev. B* **89** 205122
- [19] Sai N, Fennie C J and Demkov A A 2009 *Phys. Rev. Lett.* **102** 107601
- [20] Dagotto E, Hotta T and Moreo A 2001 *Phys. Rep.* **344** 1–135
- [21] Hu S, Chen L, Wu Y, Yu L, Zhao X, Cao S, Zhang J and Ren W 2014 *Chin. Sci. Bull.* **59** 5170
- [22] Coey M 2004 *Nature* **430** 155–6
- [23] Hill N A 2000 *J. Phys. Chem. B* **104** 6694–709
- [24] Rondinelli J M and Fennie C J 2012 *Adv. Mater.* **24** 1961–8
- [25] Filippetti A and Hill N A 2002 *J. Magn. Magn. Mater.* **242** 976
- [26] Zhu W, Pi L, Tan S and Zhang Y H 2012 *Appl. Phys. Lett.* **100** 052407
- [27] Xu X S and Wang W B 2014 *Mod. Phys. Lett. B* **28** 1430008
- [28] Wang W B et al 2013 *Phys. Rev. Lett.* **110** 237601
- [29] Disseler S M et al 2015 *Phys. Rev. Lett.* **114** 217602
- [30] Lin L et al 2016 *Phys. Rev. B* **93** 075146
- [31] Masuno A, Ishimoto A, Moriyoshi C, Hayashi N, Kawaji H, Kuroiwa Y and Inoue H 2013 *Inorg. Chem.* **52** 11889
- [32] Disseler S M et al 2015 *Phys. Rev. B* **92** 054435
- [33] Arima T, Tokunaga A, Goto T, Kimura H, Noda Y and Tokura Y 2006 *Phys. Rev. Lett.* **96** 097202
- [34] Kagawa F, Mochizuki M, Onose Y, Murakawa H, Kaneko Y, Furukawa N and Tokura Y 2009 *Phys. Rev. Lett.* **102** 057604
- [35] Sergienko I A and Dagotto E 2006 *Phys. Rev. B* **73** 094434
- [36] Katsura H, Nagaosa N and Balatsky A V 2005 *Phys. Rev. Lett.* **95** 057205
- [37] Kimura T 2007 *Annu. Rev. Mater. Res.* **37** 387–413
- [38] Goto T, Kimura T, Lawes G, Ramirez A P and Tokura Y 2004 *Phys. Rev. Lett.* **92** 257201
- [39] Dong S, Yu R, Yunoki S, Liu J M and Dagotto E 2008 *Phys. Rev. B* **78** 155121
- [40] Dong S and Liu J M 2012 *Mod. Phys. Lett. B* **26** 1230004
- [41] Hur N, Park S, Sharma P A, Ahn J S, Guha S and Cheong S W 2004 *Nature* **429** 392–5
- [42] Chapon L C, Blake G R, Gutmann M J, Park S, Hur N, Radaelli P and Cheong S W 2004 *Phys. Rev. Lett.* **93** 177402
- [43] Lee N, Vecchini C, Choi Y J, Chapon L C, Bombardi A, Radaelli P G and Cheong S W 2013 *Phys. Rev. Lett.* **110** 137203
- [44] Zhao Z Y, Liu M F, Li X, Lin L, Yan Z B, Dong S and Liu J M 2014 *Sci. Rep.* **4** 3984
- [45] Taniguchi K, Abe N, Takenobu T, Iwasa Y and Arima T 2006 *Phys. Rev. Lett.* **97** 097203
- [46] Heyer O, Hollmann N, Klassen I, Jodlauk S, Bohatý L, Becker P, Mydosh J A, Lorenz T and Khomskii D 2006 *J. Phys.: Condens. Matter* **18** L471–5
- [47] Zhang G Q, Dong S, Yan Z B, Guo Y Y, Zhang Q F, Yunoki S, Dagotto E and Liu J M 2011 *Phys. Rev. B* **84** 174413
- [48] Johnson R D, Chapon L C, Khalyavin D D, Manuel P, Radaelli P G and Martin C 2012 *Phys. Rev. Lett.* **108** 067201
- [49] Lu X Z, Whangbo M H, Dong S, Gong X G and Xiang H J 2012 *Phys. Rev. Lett.* **108** 187204
- [50] Kimura T, Sekio Y, Nakamura H, Siegrist T and Ramirez A P 2008 *Nat. Mater.* **7** 291–4
- [51] Yamasaki Y, Miyasaka S, Kaneko Y, He J P, Arima T and Tokura Y 2006 *Phys. Rev. Lett.* **96** 207204
- [52] Lawes G et al 2005 *Phys. Rev. Lett.* **95** 087205
- [53] Liu M F et al 2017 *Phys. Rev. B* **95** 195134
- [54] Holbein S et al 2016 *Phys. Rev. B* **94** 104423
- [55] Sergienko I A, Şen C and Dagotto E 2006 *Phys. Rev. Lett.* **97** 227204

- [56] Choi Y J, Yi H T, Lee S, Huang Q, Kiryukhin V and Cheong S W 2008 *Phys. Rev. Lett.* **100** 047601
- [57] Nakamura M, Tokunaga Y, Kawasaki M and Tokura Y 2011 *Appl. Phys. Lett.* **98** 082902
- [58] Dong S, Liu J M and Dagotto E 2014 *Phys. Rev. Lett.* **113** 187204
- [59] Caron J M, Neilson J R, Miller D C, Arpino K, Llobet A and McQueen T M 2012 *Phys. Rev. B* **85** 180405
- [60] Nambu Y *et al* 2012 *Phys. Rev. B* **85** 064413
- [61] Saparov B, Calder S, Sipos B, Cao H B, Chi S X, Singh D J, Christianson A D, Lumsden M D and Sefat A S 2011 *Phys. Rev. B* **84** 245132
- [62] Medvedev M V, Nekrasov I A and Sadovskii M V 2012 *JETP Lett.* **95** 37–41
- [63] Luo Q *et al* 2013 *Phys. Rev. B* **87** 024404
- [64] Zhang Y, Lin L F, Zhang J J, Dagotto E and Dong S 2018 *Phys. Rev. B* **97** 045119
- [65] Caron J M, Neilson J R, Miller D C, Llobet A and McQueen T M 2011 *Phys. Rev. B* **84** 180409
- [66] Lovesey S W, Khalyavin D D and van der Laan G 2016 *Phys. Scr.* **91** 015803
- [67] Li W, Dong S, Fang C and Hu J P 2012 *Phys. Rev. B* **85** 100407
- [68] Li W *et al* 2012 *Nature Phys.* **8** 126–30
- [69] Li W *et al* 2012 *Phys. Rev. Lett.* **109** 057003
- [70] Zhang Y, Zhang H M, Weng Y K, Lin L F, Yao X Y and Dong S 2016 *Phys. Status Solidi* **10** 757–61
- [71] Dai P C 2015 *Rev. Mod. Phys.* **87** 855–96
- [72] de la Cruz C *et al* 2008 *Nature* **453** 899–902
- [73] Selivanov E N, Chumarev V M, Gulyaeva R I, Mar'evich V P, Vershinin A D, Pankratov A A and Korepanova E S 2004 *Inorg. Mater.* **40** 845–50
- [74] Sambrook T, Smura C F and Clarke S J 2007 *Inorg. Chem.* **46** 2571–4
- [75] Jin S F, Huang Q, Lin Z P, Li Z L, Wu X Z, Ying T P, Wang G and Chen X L 2015 *Phys. Rev. B* **91** 094420
- [76] Delacotte C, Pérez O, Pautrat A, Berthebaud D, Hébert S, Suard E, Pelloquin D and Maignan A 2015 *Inorg. Chem.* **54** 6560–5
- [77] Zhang Y, Lin L F, Zhang J J, Huang X, An M and Dong S 2017 *Phys. Rev. Mater.* **1** 034406
- [78] Yu L and Zunger A 2012 *Phys. Rev. Lett.* **108** 068701
- [79] Yu L P, Kokenyesi R S, Keszler D A and Zunger A 2013 *Adv. Energy Mater.* **3** 43–8
- [80] Yin W J, Kokenyesi T T, Keszler D A and Zunger A 2014 *Adv. Mater.* **26** 4653–8
- [81] Ikeda N *et al* 2005 *Nature* **436** 1136–8
- [82] Subramanian M, He T, Chen J, Rogado N, Calvarese T and Sleight A 2006 *Adv. Mater.* **18**
- [83] Nagano A, Naka M, Nasu J and Ishihara S 2007 *Phys. Rev. Lett.* **99** 217202
- [84] Xiang H J and Whangbo M H 2007 *Phys. Rev. Lett.* **98** 246403
- [85] Zhang Y, Yang H X, Ma C, Tian H F and Li J Q 2007 *Phys. Rev. Lett.* **98** 247602
- [86] Alexe M, Ziese M, Hesse D, Esquinazi P, Yamauchi K, Fukushima T, Picozzi S and Gösel U 2009 *Adv. Mater.* **21** 4452–5
- [87] de Groot J, Mueller T, Rosenberg R A, Keavney D J, Islam Z, Kim J W and Angst M 2012 *Phys. Rev. Lett.* **108** 187601
- [88] Niermann D, Waschowski F, de Groot J, Angst M and Hemberger J 2012 *Phys. Rev. Lett.* **109** 016405
- [89] Angst M 2013 *Phys. Status Solidi* **7** 383
- [90] Fonin M, Pentcheva R, Dedkov Y S, Sperlich M, Vyalikh D V, Scheffler M, Rüdiger U and Güntherodt G 2005 *Phys. Rev. B* **72** 104436
- [91] Liu X H, Chang C F, Rata A D, Komarek A C and Tjeng L H 2016 *NPJ Quantum Mater.* **1** 16027
- [92] Lin L F, Xu Q R, Zhang Y, Zhang J J, Liang Y P and Dong S 2017 *Phys. Rev. Mater.* **1** 071401
- [93] Greenwood N N, Howe A T and Menil F 1971 *J. Chem. Soc. A* **0** 2218–24
- [94] Fourquet J L, Samedi E L and Calage Y 1988 *J. Solid State Chem.* **77** 84
- [95] Shachar G, Makovsky J and Shaked H 1972 *Phys. Rev. B* **6** 1968–74
- [96] Wintenberger M M, Tressaud M A and Menil F 1972 *Solid State Commun.* **10** 739